European Journal of Medicinal Chemistry 275 (2024) 116638

Contents lists available at ScienceDirect

European Journal of Medicinal Chemistry

journal homepage: www.elsevier.com/locate/ejmech

Research paper

Self-assembly of a ruthenium-based cGAS-STING photoactivator for carrier-free cancer immunotherapy

Yu-Yi Ling [a,b,1], Zhi-Yuan Li [a,b,1], Xia Mu [c,1], Ya-Jie Kong [a,b], Liang Hao [a,b], Wen-Jin Wang [a,b], Qing-Hua Shen [a,b], Yue-Bin Zhang [c,**], Cai-Ping Tan [a,b,*]

[a] MOE Key Laboratory of Bioinorganic and Synthetic Chemistry, Sun Yat-Sen University, Guangzhou, 510006, PR China
[b] Guangdong Basic Research Center of Excellence for Functional Molecular Engineering, Guangzhou, 510006, PR China
[c] State Key Laboratory of Molecular Reaction, Dynamics, Dalian Institute of Chemical Physics, Chinese Academy of Sciences, Dalian, 116023, PR China

ARTICLE INFO

Handling Editor: Dr. Z Liu

Keywords:
cGAS-STING
Self-assembly
Ru(II) complexes
DNA binding
Photoimmunotherapy

ABSTRACT

The cGAS (cyclic GMP-AMP synthase)-STING (stimulator of interferon genes) pathway promotes antitumor immune responses by sensing cytosolic DNA fragments leaked from nucleus and mitochondria. Herein, we designed a highly charged ruthenium photosensitizer (**Ru1**) with a β-carboline alkaloid derivative as the ligand for photo-activating of the cGAS-STING pathway. Due to the formation of multiple non-covalent intermolecular interactions, **Ru1** can self-assemble into carrier-free nanoparticles (NPs). By incorporating the triphenylphosphine substituents, **Ru1** can target and photo-damage mitochondrial DNA (mtDNA) to cause the cytoplasmic DNA leakage to activate the cGAS-STING pathway. Finally, **Ru1** NPs show potent antitumor effects and elicit intense immune responses *in vivo*. In conclusion, we report the first self-assembling mtDNA-targeted photosensitizer, which can effectively activate the cGAS-STING pathway, thus providing innovations for the design of new photo-immunotherapeutic agents.

1. Introduction

Since 2008, Barber et al. identify STING (stimulator of interaction genes) as a vital component of host innate immunity, it is found to show substantial capacity in virus/bacterial/parasitic infections and cancer immunity by regulating protein synthesis and interferon (IFN) expression [1,2]. Double-stranded DNA (dsDNA) induces the activation of cyclic GMP-AMP synthase (cGAS) [3–6]. Upon binding dsDNA, the dimerization of cGAS leads to its enzyme activation and the synthesis of 2′-3′-cyclic GMP-AMP (cGAMP) [7,8]. cGAMP binds to the dimer of STING located on the endoplasmic reticulum (ER) membrane, leading to conformational changes and oligomerization of STING [3,9]. Then, STING promotes the autophosphorylation of TANK binding kinase 1 (TBK1) and recruit interferon regulatory factor 3 (IRF3) [10,11]. The TBK1 phosphorylates IRF3, which leads to the dimerization and translocation of IRF3 to the nucleus to induce the expression of type I IFN, Interferon-stimulated gene (ISG) and several other inflammatory mediators and chemokines [12].

The activation of cGAS-STING cascade can release immune-stimulatory factors to attenuate tumour growth and recruit immune cells for tumour suppression [13,14]. Moreover, STING-IRF3-induced type I interferon production can induce tumour antigen presentation on dendritic cells and macrophages for cross-priming of $CD8^+$ T cells [15,16]. The cGAS-STING pathway can be activated by cytosolic dsDNA with exogenous origins or endogenous genomic and mitochondrial DNA (mtDNA) [17,18]. Multiple strategies have been developed to activate the STING pathway in tumour cells or tumour infiltrating immune cells [19,20]. Based on the typical molecular mechanisms, STING agonists or nanocarriers, as well as induction of mitochondrial and nuclear dsDNA release, can activate the cGAS-STING signaling pathway [21]. Most of the agents currently in clinical trials are cyclic dinucleotide (CDN) derivatives mimicking cGAMP, which are hindered by their high molecular weight, poor membrane permeability, and poor stability [22]. Non-CDN agonists, e.g., diABZI-Compound 3 from GSK [23], SR717 from Scripps Research [24], MSA-2 from Merck [25], and NVS-STG2 from Novartis [26], exhibit encouraging efficacy *in vitro* and *in vivo*. However, the

* Corresponding author. MOE Key Laboratory of Bioinorganic and Synthetic Chemistry, Sun Yat-Sen University, Guangzhou 510006, PR China.
** Corresponding author.
E-mail addresses: zhangyb@dicp.ac.cn (Y.-B. Zhang), tancaip@mail.sysu.edu.cn (C.-P. Tan).
[1] These authors contributed equally to this work.

https://doi.org/10.1016/j.ejmech.2024.116638
Received 4 May 2024; Received in revised form 21 June 2024; Accepted 27 June 2024
Available online 28 June 2024

systemic administration of STING agonists may induce "cytokine storm" to damage normal tissues, which limits their further clinical use [17], To resolve these issues, the tumour-targeted delivery agents of STING agonists, e.g., nanoscale coordination polymers [27], polymer-based platform [28–30], lanthanide-nucleotide coordination nanoparticles [31] and nucleotide nanocomplex-decorated ultrasound microbubbles [32,33], have been developed.

Compared with traditional cancer therapy, photodynamic therapy (PDT) has attracted extensive attention as it is non-invasive [34–36]. PDT uses photosensitizers (PSs) to transfer energy from light to oxygen in the tumour, thus producing highly cytotoxic reactive oxygen species (ROS), leading to tumour tissue necrosis or apoptosis [35]. Among the transition metal-based photosensitizers studied at present, Ru(II) polypyridine complexes are the most attractive candidates, which can be ascribed to their long excited state lifetimes, effective $^1O_2$ sensitization, visible light absorption, high cell penetration capability and two/multi-photon absorptions [37,38]. In particular, the Ru(II) based photosensitizer TLD1433 developed by McFarland and her colleagues has entered clinical trials for bladder cancer treatment [39]. Because PSs are not easy to accumulate in tumor tissues, it is difficult for PSs to accurately target cancer cells [40]. A variety of nanomaterials (including peptides and polymer/inorganic materials) have been used for PS delivery to enhance tumor targeting and blood circulation time [41–43]. Due to the enhanced permeability and retention (EPR) effect, the nanoparticles can accumulate in tumor tissues to improve the accuracy and efficiency of PDT and minimize the off-targeted effects [44]. However, the nanocarriers also have many disadvantages, including complex manufacturing, poor stability after dilution, limited drug loading, premature drug release and potential toxicity [45]. In recent years, carrier free self-assembled nanomedicine/photosensitizers constructed through tuning of non-covalent intermolecular interactions have attracted attention due to the ease of preparation and less susceptibility to unexpected side effects [46–49].

Previously, we found that mtDNA damage can stimulate the cGAS-STING pathway [50,51]. Considering the carrier-free strategy based on self-assembly is helpful to avoid the toxicity of the carrier, and photo-induced mtDNA damage can achieve the temporal and spatial control of cGAS-STING activation, we designed a ruthenium complex (**Ru1**) containing two ancillary ligands with triphenylphosphine modified alkyl chains and a main ligand of a bioactive β-carboline alkaloid derivative (Scheme 1). As it can form multivalent intermolecular interactions, **Ru1** can self-assemble into stable nanoparticles. Due to the presence of the highly charged triphenylphosphine groups, **Ru1** can target mitochondria. Upon light irradiation, **Ru1** can damage mtDNA to cause cytoplasmic dsDNA release for the activation of the cGAS-STING pathway both *in vitro* and *in vivo* (Scheme 1). In summary, we propose a strategy for designing self-assembled cGAS-STING activators, which may provide ideas for the design of novel photo-immunotherapeutic agents.

2. Results and discussion

2.1. Synthesis and characterization

Ru1 was synthesized by reacting the precursor *cis*-[Ru(DMSO)$_2$Cl$_2$] (DMSO = Dimethyl sulfoxide) with 1 equiv of 1-(2-pyridyl)-β-carboline) (**1-Py-βC**) and 2 equiv of (6-(1,10-phenanthroline-5-carboxamido) hexyl)triphenylphosphonium (**phen-PPh$_3$**) at 140 °C for 6 h, followed by purification by silica chromatography (Scheme S1, Supporting Information). The control compound **Ru2** was synthesized by reacting the precursor *cis*-[Ru(phen)$_2$Cl$_2$] (phen = 1,10-phenanthroline) with the ligand **1-Py-βC** and purified by silica chromatography as previously described [52]. **Ru1** and **Ru2** were characterized by ESI-MS, ^{1}H NMR spectroscopy, ^{13}C NMR spectroscopy and HPLC (Figs. S1–S11).

The absorption spectra of **Ru1** and **Ru2** are characterized by intense spin-allowed intraligand (^{1}IL) absorption bands in the UV region at ca. 250–340 nm and less intense spin-allowed metal-to-ligand charge transfer (^{1}MLCT) absorption bands at ca. 350–530 nm, which are typical absorption properties of Ru(II) polypyridine complexes (Fig. 1A and S12) [52]. **Ru1** and **Ru2** show strong fluorescence emission when excited at 450 nm, and the maximum emission peak is about 620 nm (Fig. 1B and S13). The emission quantum yields of **Ru1** and **Ru2** in phosphate buffered saline (PBS), CH_3CN and CH_2Cl_2 fall in the range between 0.038 and 0.077 (Table S1). UV/vis spectroscopy monitoring shows that **Ru1** and **Ru2** are stable upon irradiation with a 425 nm laser for 30 min in PBS (pH 7.4, Fig. S14). The quantum yields of **Ru1** and **Ru2** to photosensitize the generation of singlet oxygen ($^1O_2$) are (0.274 ± 0.022) and (0.163 ± 0.006), respectively (Fig. 1B). Upon the addition of sodium azide (NaN_3), a known $^1O_2$ quencher, the quantum yields of $^1O_2$ for **Ru1** and **Ru2** were decreased to (0.160 ± 0.006) and (0.074 ± 0.012), respectively, further indicating that **Ru1** has the stronger photodynamic effect than **Ru2**.

2.2. Self-assembly of Ru1 enhances the cellular uptake efficacy and PDT activities

The PDT activities of **Ru1** and **Ru2** *in vitro* were evaluated in human triple negative breast cancer (TNBC) MDA-MB-231 cells, mouse TNBC 4T1 cells, human normal breast epithelial MCF-10 A cells and human cervical cancer Hela cells (Table 1 and S2). With IC_{50} values being higher than 50 μM, both **Ru1** and **Ru2** can be considered to be nontoxic in dark. In the presence of light, the IC_{50} values of **Ru1** drop to about 0.5

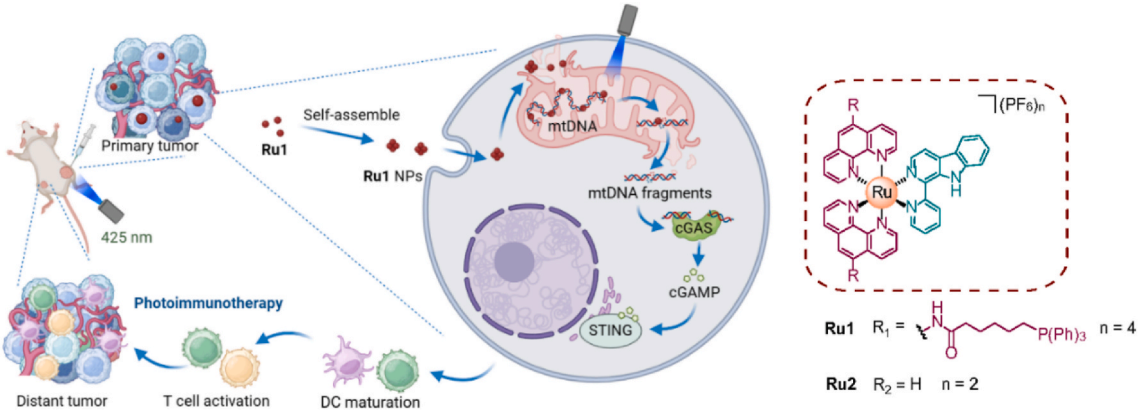

Scheme 1. Action mechanisms of **Ru1** and chemical structures of **Ru1** and **Ru2**. **Ru1** can self-assemble into carrier-free NPs, penetrate into cancer cells through endocytosis, and effectively target mitochondrial and reside in tumour tissue. Upon light irradiation, **Ru1** can damage mtDNA, leading to the cytoplasmic DNA release, thereby activating the cGAS-STING pathway and causing dendritic cells (DCs) maturation and T cell activation. Created with BioRender.com.

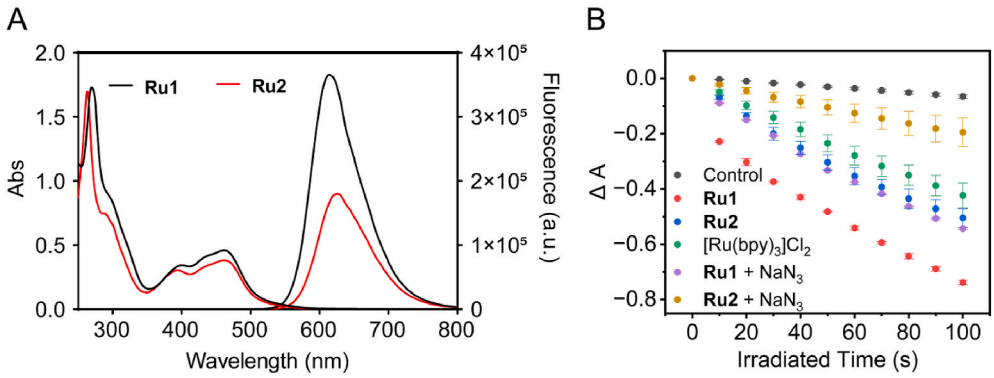

Fig. 1. (A) UV/Vis absorption spectra and emission spectra of **Ru1**/**Ru2** (20 μM) measured in degassed PBS buffer (pH 7.4, with 1 % DMSO) at 298 K. $\lambda_{ex} = 450$ nm. (B) The capability of **Ru1**/**Ru2** (20 μM) to photosensitize the generation of $^1O_2$ probed by 9,10-anthracenediyl-bis(methylene) dimalonic acid (ABDA, 100 μM) in degassed PBS buffer (pH 7.4, with 1 % DMSO) at 298 K, using NaN_3 (5 mM) as the $^1O_2$ quencher and $[Ru(bpy)_3]Cl_2$ (bpy: 2,2′-bipyridine) as the standard.

Table 1
IC_{50} (μM, 48 h) values of **Ru1** and **Ru2** towards TNBC cell lines.

Compounds	MDA-MB-231			4T1		
	Dark	Light	PI	Dark	Light	PI
Ru1	>50	0.5 ± 0.05	>100	36.9 ± 2.1	2.7 ± 0.5	13.7
Ru2	>50	1.0 ± 0.08	>50	>50	33.9 ± 2.9	>1.5
Cisplatin	11.2 ± 0.8	8.7 ± 0.7	1.29	13.5 ± 2.6	13.6 ± 1.8	1.0

[a] Data are presented as the mean ± standard deviation (SD), and cells were incubated with the tested compounds for 48 h and detected by MTT assay.
[b] Cells were incubated with the compounds for 24 h in the dark and then irradiated with a 425 nm laser (12 J cm^{-2}).
[c] PI is the ratio of the IC_{50} value in the dark to that obtained upon light irradiation.

μM and 2.7 μM in MDA-MB-231 and 4T1 cells, respectively. The photocytotoxicity index (PI) values of **Ru1** is higher than **Ru2**, especially in 4T1 cells. As expected, light irradiation doesn't show profound effects on the antiproliferative activities of cisplatin. Meanwhile, **Ru1** and **Ru2** show relatively lower photocytotoxicities in MCF-10 A cells and HeLa cells (Table S2), implying their selective antitumor effects towards TNBC cells.

Interestingly, **Ru1** can self-assemble into nanoparticles in PBS, while **Ru2** cannot (Fig. 2A). Transmission electron microscopy (TEM) shows that **Ru1** forms nanoparticles with a uniform spherical morphology and an average size of around 30 nm (Fig. 2A), which is smaller than that detected by dynamic light scattering (DLS; about 125 nm; Fig. 2B).

Molecular dynamics (MD) simulations were further conducted to investigate the mechanism of self-assembly of **Ru1** molecules into nanoparticles. We constructed an initial MD simulation system consisting of 72 **Ru1** molecules (6 × 6 × 2) with a spacing of 20 Å (Fig. S15 A). In addition, a comparison system with the presence of 30 NaH_2PO_4 molecules was also built to mimic the PBS buffer used in our experimental study (Fig. S15 B). Four independent MD simulations of each system were performed lasting for 1500 ns and the MD trajectories from 500–1500 ns were used for analysis. The radial distribution functions (RDFs) for the distance between Ru–Ru atoms were utilized to evaluate the degree of aggregation (Fig. 2C). In the absence of NaH_2PO_4 molecules, the RDF exhibits two peaks at 9.0 Å and 12.0 Å, respectively. In sharp contrast, the presence of NaH_2PO_4 molecules significantly enhanced the aggregation. Three prominent peaks would be easily identified around 9.2 Å, 11.2 Å, and 13.3 Å. A representative snapshot illustrates the spatial geometry corresponding to the three peaks (Fig. 2D). The RDF at 9.2 Å demonstrates π-π conjugation interactions between the phenanthroline groups of two **Ru1** molecules, while at 11.2 Å, the cluster is stabilized via the p-π interactions between the β-carboline group and the alkyl chain. The largest peak is located at 13.3 Å, where the cluster is maintained via both π-π stacking interactions of two β-carboline groups and p-π interactions between β-carboline and alkyl chain, indicating the indispensable role of the β-carboline group for self-assembly.

The formation of self-assembled nanoparticles may enhance the cellular uptake efficacy and the tumor penetration and retention effects [46,49]. ICP-MS experiment shows that during an incubation period of 6 h, the cellular content of **Ru1** gradually increases, and its accumulation in mitochondria is more pronounced compared to that in cytoplasm (Fig. 2E). In contrast, the cellular uptake level and the concentration in mitochondria of **Ru2** cells are significantly lower than those of **Ru1**. In order to further verify that the higher cellular uptake level of **Ru1** is due to the formation of NPs, we studied the cellular uptake mechanism of **Ru1** and **Ru2** using different inhibitors [50]. After being pretreated with the endocytosis inhibitor chloroquine (CQ), the amount of ruthenium in MDA-MB-231 cells is decreased distinctly, while being incubated at 4 °C doesn't significantly affect the cellular ruthenium contents (Fig. 2F). The uptake of **Ru1** is energy-dependent endocytosis, mainly mediated by clathrin, while the uptake of **Ru2** is energy independent passive diffusion according to our previous reports [52]. Meanwhile, being incubated at 4 °C or pretreated with CQ, the amount of ruthenium in MCF-10 A cells is decreased markedly (Fig. S16), which indicates that **Ru1** penetrates into normal cells through energy-dependent endocytosis.

2.3. *Ru1 can induce the aggregation of dsDNA*

Since β-carboline derivatives have been proven to be effective DNA binding agent [53], and our previous work has proved that Ru(II) complexes with triphenylphosphine-substituted ligands can induce changes in the aggregation states of DNA [54], we then studied the binding properties of **Ru1** with DNA. The absorbance of **Ru1** at about 260 nm decreases, and the absorbance around 470 nm increases, which suggests that **Ru1** may induce DNA aggregation [55]. The calculated binding constant of **Ru1** towards calf thymus-DNA (CT-DNA) obtained by UV–vis titration is 1.22×10^6 M^{-1} (Fig. 3A). In the presence of CT-DNA, the emission intensity of **Ru1** is slightly increased by 1.5-fold (Fig. 3B). The calculated binding constant of **Ru1** towards CT-DNA obtained by fluorescence titration is 3.63×10^5 M^{-1}. The circular dichroism (CD) spectroscopy of CT-DNA incubated with **Ru1** show an obvious increase in the molar ellipticity of positive bands around 275 nm, which can be attributed to the base pair stacking, indicating that intercalative binding mode of **Ru1** with CT-DNA alters secondary structure of duplex DNA [56]. The blue shift of positive bands and the appearance of the negative band at 280 nm imply a significant change in CT-DNA conformation [57]. Consistent with our previous findings [54],

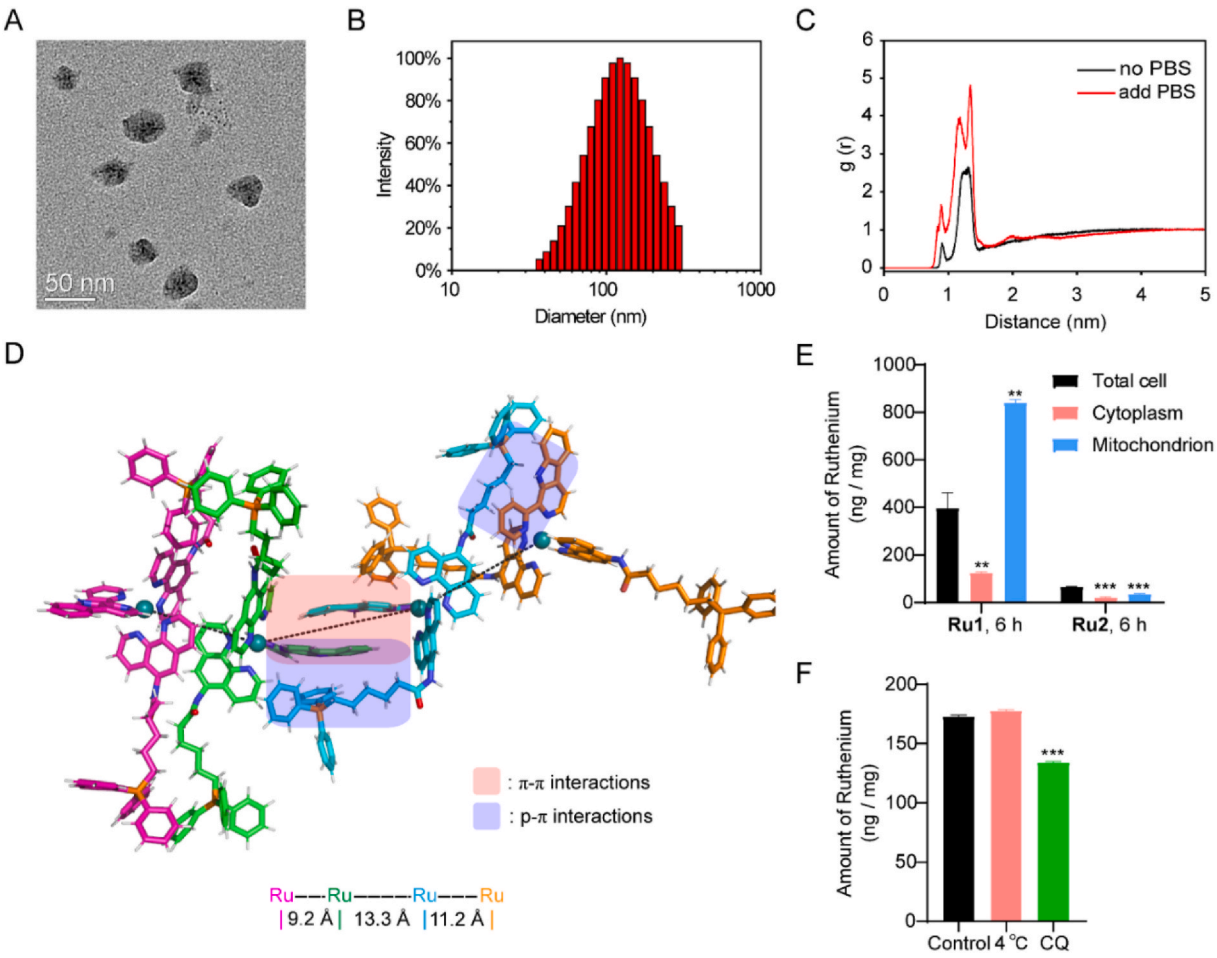

Fig. 2. **Ru1** can self-assemble into nanoparticles and penetrate into cancer cells by endocytosis. (A) TEM images of the NPs formed by **Ru1** in PBS buffer (pH 7.4). Scale bar: 50 nm. (B) DLS analysis of the NPs formed by **Ru1** in PBS buffer (pH 7.4). (C) Radial distribution functions for the distances between Ru–Ru atoms with (red line)/without (black line) NaH_2PO_4 molecules. (D) A representative snapshot to illustrate the key interactions within the cluster. (E) Content of Ru per milligram of protein and their intracellular compartment distribution in MDA-MB-231 cells. The cells were incubated with **Ru1**/**Ru2** (20 μM) for 6 h. (F) Content of Ru per milligram of protein and their intracellular compartment distribution in MDA-MB-231 cells. The cells were incubated with **Ru1** (20 μM) and different inhibitors. Error bars: S.D., n = 3. $^{*}p < 0.05$, $^{**}p < 0.01$, $^{***}p < 0.001$.(For interpretation of the references to colour in this figure legend, the reader is referred to the web version of this article.)

the highly charged **Ru1** complexes can induce DNA aggregation under dark conditions (Fig. 3D and S17). At higher concentrations (>15 μM), the negative charge on DNA is neutralized by **Ru1**, and the **Ru1**-DNA complex moves towards the negative electrode. In the presence of light, **Ru1** can efficiently cleavage DNA from supercoiled to nicked form at a concentration of 1 μM (Fig. 3E and S17).

MD simulations were employed to further understand the molecular basis responsible for the aggregation of DNA segments induced by **Ru1**. Three single insertions of **Ru1** at different positions were built for in-silicon studies (Fig. S18), including the AT pair closing to the terminal of DNA segment (AT-DNA; I; Fig. 3F), the CG pair near the other terminal of DNA segment (CGd-DNA; II) and the CG pair in the middle of the DNA (CGm-DNA; III). Furthermore, three **Ru1** molecules inserted into the DNA segments at the positions of I, II, and III were constructed and named AT-CGd-CGm-DNA. A system with only 15 copies of DNA segments was also modeled for comparison (Fig. 3G).

The initial MD conformation consists of 15 copies of DNA segments separated by 40 Å, and the DNA aggregation process is indicated by the decrease in the total number of clusters (Figs. S19–S22). Due to the finite size of our MD simulation system with periodic boundary conditions (PBC), the aggregation process occurs during the first 400 ns in all of our MD simulation systems. The total number of clusters begins to decrease from 15 and reaches equilibrium after 400 ns. Furthermore, the distribution analysis using the last 500 ns of MD trajectories from the clustering profiles clearly shows an enhancement of aggregation propensity after the insertion of **Ru1**. Especially, one of our simulated MD trajectories of the AT-CGd-CGm-DNA system manifests that all DNA segments are connected to each other and form a single large cluster after 500 ns MD simulations, suggesting an additive effect of **Ru1** insertion to induce DNA aggregation (Fig. 3F and S23).

In the DNA-only MD simulation system, the interactions between DNA segments are predominantly contributed by end-to-end stacking at the terminals, forming reversible linear aggregates (Fig. 3G). Upon the insertion of **Ru1**, two additional interaction patterns are observed. The first interaction pattern is a T-shaped pattern arising from the interaction between the tail group of one DNA segment inserted by **Ru1** molecule and the terminal base of the other DNA segment (Fig. 3H). The second interaction pattern is the inter-molecular interactions of **Ru1**, especially the interactions between the $P(Ph)_3$ groups (Fig. S24). The T-shaped pattern is well maintained during the MD simulations, while the later interactions are dynamic and interchangeable due to the flexibility of the long alkyl chain.

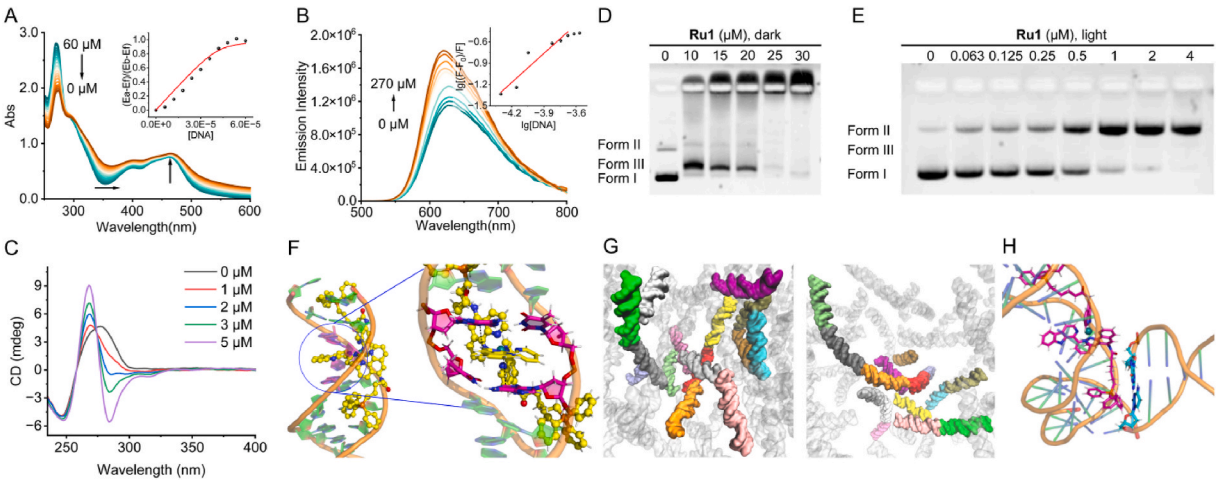

Fig. 3. Binding properties of **Ru1** with DNA. (A and B) UV–vis titration and fluorescence titration of **Ru1** (30.0 μM) with CT-DNA in Tris-HCl buffer (pH 7.4, with 1 % DMSO). The arrows show the changes in the absorbance upon addition of CT-DNA. (C) CD spectroscopy of dsDNA in Tris-HCl buffer (pH 7.4, 100 mM NaCl) in the presence of different concentrations **Ru1**. (D and E) Agarose gel electrophoresis of pBR322 plasmid (4361 bp; 10 ng uL^{-1}) in the absence and presence of light (12 J cm^{-2}, i.e. 20 mW cm^{-2} for 10 min). DNA was incubated different concentrations of **Ru1**. Form I/II/III: supercoiled/nicked/linear DNA. (F) MD-simulated binding structure of **Ru1** with AT-DNA. The mainchain of DNA is shown in green, the upper and lower layers of β-carboline are labelled in purple. **Ru1** is shown in yellow sphere-sticks. (G) Snapshots of DNA aggregation in AT-CGd-CGm-DNA model (left panel) and DNA-only model (right panel), DNA segments located in the periodic images are shown in white surface representations. (H) The stabilization of T-shaped binding arises from the p-π interaction between the long alkyl chain and the terminal base pair of DNA.(For interpretation of the references to colour in this figure legend, the reader is referred to the web version of this article.)

2.4. Ru1 NPs can activate cGAS-STING pathway by photo-damaging mtDNA

Ru1-mediated PDT causes a dose-dependent increase in the cellular ROS levels as measured by 2′,7′-dichlorodihydrofluorescein diacetate (DCFH-DA) staining and flow cytometry (Fig. 4A). At a concentration of 1.5 μM, **Ru1**-mediated PDT results in an approximately 20-fold increase in cellular ROS levels. After **Ru1** treatment in the presence light, most cells show depolarized mitochondrial with lost mitochondrial membrane potential (MMP), as evidenced by 5,5′,6,6′-tetrachloro-1,1′,3,3′-

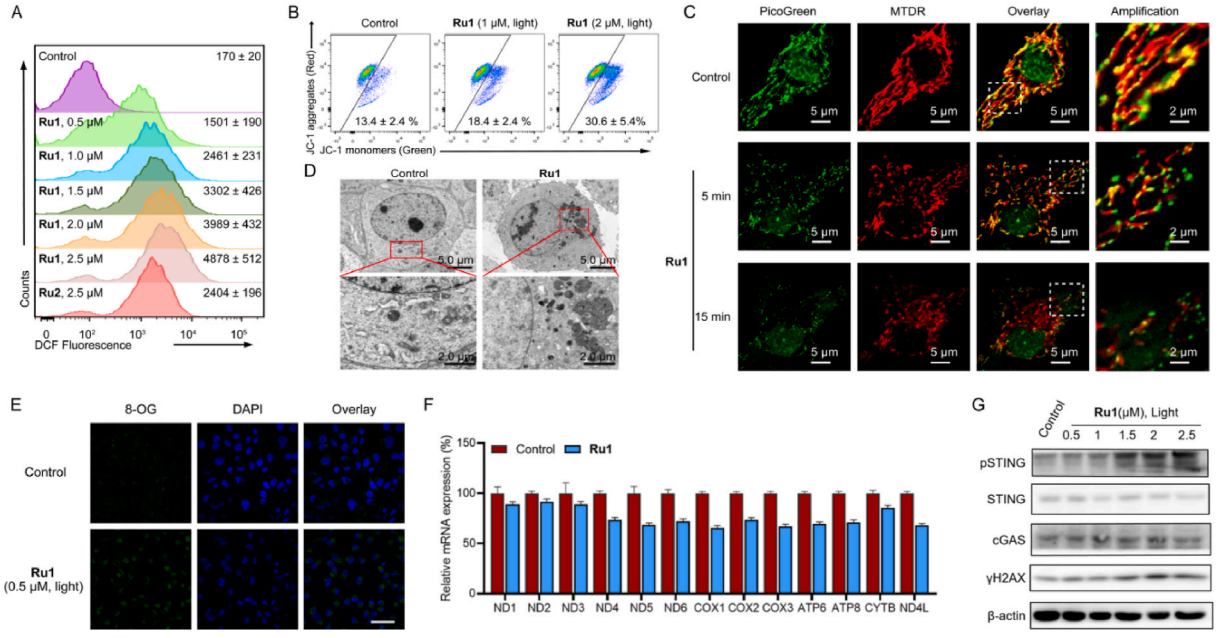

Fig. 4. (A) Flow cytometry measurement of cellular ROS in MDA-MB-231 cells treated with **Ru1** at the indicated concentrations for 12 h in the presence of light (425 nm; 12 J cm^{-2}). (B) Impact of **Ru1** on MMP measured by JC-1 staining and flow cytometry. $\lambda_{ex} = 488$ nm; $\lambda_{em} = 530 \pm 30$ nm (Green)/590 ± 30 nm (Red). MDA-MB-231 cells were treated with **Ru1** at the indicated concentrations for 12 h in the presence of light (425 nm, 12 J cm^{-2}). (C) Confocal images of **Ru1**-treated MDA-MB 231 cells stained with PicoGreen and MTDR for 15 min. Cells were treated with **Ru1** at the indicated concentrations for 12 h in the presence of light (425 nm, 12 J cm^{-2}). (D) TEM images of MDA-MB-231 cells treated with **Ru1** (0.5 μM) for 12 h and irradiated with a 425 nm laser (12 J cm^{-2}). (E) Immunofluorescence assay of 8-OG in MDA-MB-231 cells treated with **Ru1** at the indicated concentrations for 6 h in the presence of light (425 nm, 12 J cm^{-2}). 8-OG: $\lambda_{ex} = 488$ nm; $\lambda_{em} = 518 \pm 20$ nm. DAPI: $\lambda_{ex} = 405$ nm; $\lambda_{em} = 461 \pm 20$ nm. (F) Impact of **Ru1**-mediated PDT on the transcription levels of mitochondria-encoded genes analyzed by RT-qPCR. MDA-MB 231 cells were treated with **Ru1** (1 μM) for 12 h, irradiated with 425 nm (12 J cm^{-2}) light array. (G) Protein expression levels of cGAS-STING signaling pathway related proteins in MDA-MB-231 cells after treatment with different concentration of **Ru1** in the presence of light (425 nm, 12 J cm^{-2}).(For interpretation of the references to colour in this figure legend, the reader is referred to the web version of this article.)

tetraethylbenzimidazolyl-carbocyanine iodide (JC-1) staining (Fig. 4B). About 32 % of cells lost MMP after they are treated with **Ru1** at 2 μM upon irradiation. Morphological observation also shows that mitochondria change from a filament to dot-like pattern in cells subjected to **Ru1**-mediated PDT treatment (Fig. 4C). Meanwhile, Picogreen reveals the good colocalization with MitoTracker Deep Red (MTDR) in the control cells with a high Pearson's correlation coefficient (PCC: 0.72, Fig. S25A). After incubated with **Ru1** for 12 h and irradiated at 425 nm laser for 5 or 15 min, the localization of Picogreen was gradually separated from MTDR (PCC: 0.35 and 0.40, Figs. S25B and S25C), indicating that mtDNA was released from mitochondria. Correspondingly, Transmission electron microscope (TEM) observation shows that mitochondria in the treated cells seem to fuse together (Fig. 4D). These results show that **Ru1**-mediated PDT can significantly elevate ROS levels and affect mitochondrial functions.

Immunostaining of 8-oxoguanine (8-OG) staining shows that oxidative damage of DNA caused by **Ru1**-mediated PDT mainly occurs in mitochondria, rather than in the nuclei (Fig. 4E). Reverse transcription quantitative polymerase chain reaction (RT-qPCR) also shows that the transcription of 13 genes encoded by mtDNA is significantly downregulated in cells subjected to **Ru1**-mediated PDT (Fig. 4F).

Because mtDNA damage may lead to the release of cytoplasmic DNA, thus activating the cGAS-STING signal pathway [58], we first detected the existence of dsDNA in the cytoplasm. Picogreen staining shows that large and bright mitochondrial nucleoids form in the cytoplasm after **Ru1** treatment in combination with light (Fig. 4C), which is one of the markers of mtDNA damage [50]. The expression of the marker of DNA damage response, γH2AX is increased [59]. Accordingly, **Ru1**-mediated PDT increases the expression of cGAS and phospho-STING (pSTING; Fig. 4G and S26). These results indicate that **Ru1** can activate the cGAS-STING pathway by photo-damaging mtDNA.

2.5. Impact of Ru1 treatment on transcriptome

We further investigated the impact of **Ru1** on transcriptome by RNA-sequencing. Compared with the control group, 215 differentially expressed genes (DEGs; $|\text{fold change (FC)}| \geq 2$; false discovery rate (FDR) ≤ 0.05) were detected in cells treated with **Ru1** combined with light, of which 80 were significantly upregulated and 135 were significantly downregulated (Fig. 5A). Cluster analysis and Heatmap displays that the differentially expressed genes induced by **Ru1**-treated group show significant differences in expression patterns compared with the control group, indicating repeatability of the data (Fig. 5B).

Gene Ontology (GO) enrichment analysis shows that **Ru1**-mediated PDT mainly affects regulation of cell communication, molecular function and binding (Figs. S27–S29). Kyoto Encyclopedia of Genes and Genomes (KEGG) enrichment analysis shows that **Ru1** mainly affects the PI3K-AKT signaling pathway, Interleukin 17 (IL-17) signaling pathway, tumor necrosis factor (TNF) signaling pathway and hypoxia inducible factor 1α (HIF-1α) signaling pathway (Fig. 5C). Gene set enrichment analysis (GSEA) shows that in cells treated with **Ru1**-treated group, pathways related to translation, cellular respiration, mitochondrial electron transport, nicotinamide adenine dinucleotide (NADH) to ubiquinone and oxidation-reduction process are upregulated (Fig. 5D). The result is consistent with the fact that **Ru1** can localized in mitochondria to impact the material and energy metabolism of tumor cells, and it can also modulate the immune function of tumor cells.

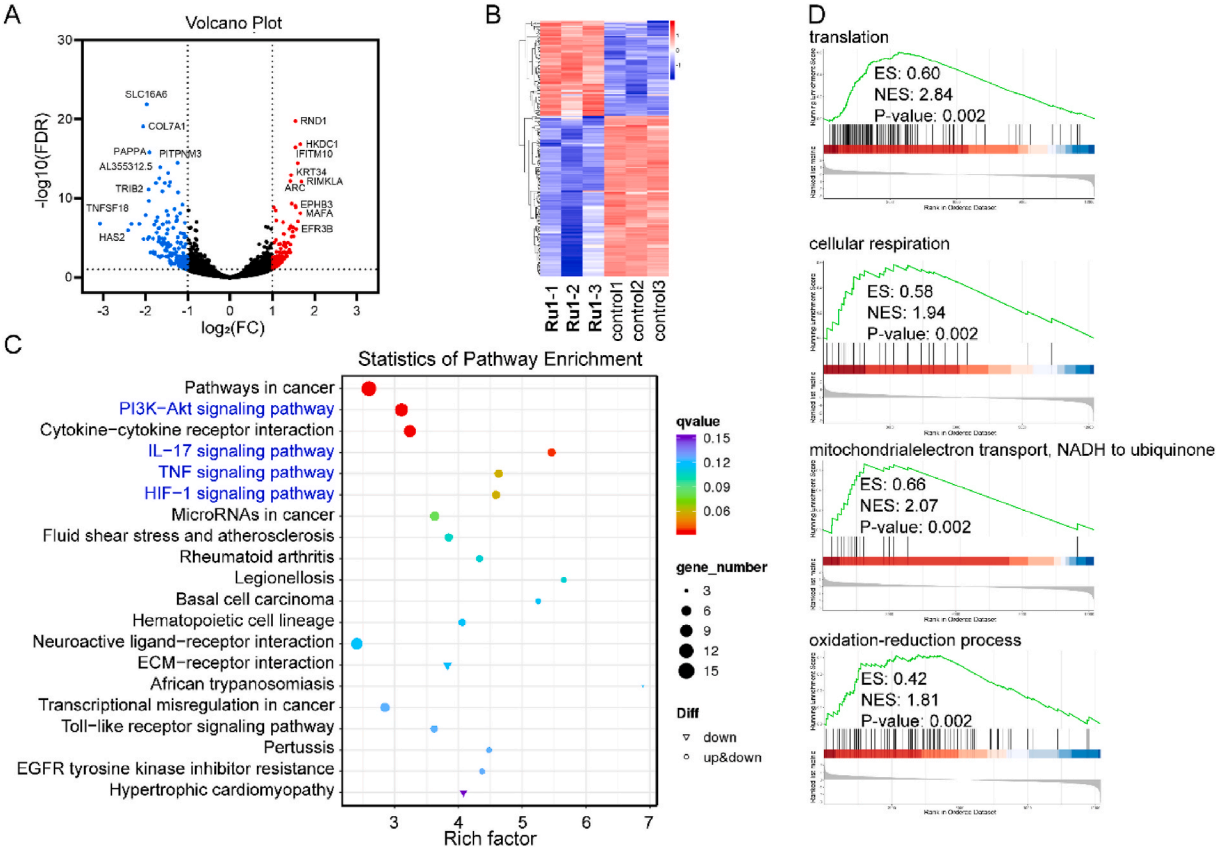

Fig. 5. Impact of **Ru1** on transcriptome. (A) Volcano plots show the differentially expressed genes in **Ru1**-treated (0.5 μM, 12 h) MDA-MB-231 cells in the presence of 425 nm laser (12 J cm^{-2}). (B) Cluster analysis and Heatmap displays the overview of the differentially expressed genes. (C) KEGG enrichment analysis of the DEGs after **Ru1**-mediated PDT treatment. (D) GSEA reveals negative and positive enrichment of genes altered in various cellular processes. NES: normalized enrichment score.

2.6. Ru1 activate cancer immune responses in vivo

In order to validate the phototherapeutic effects of **Ru1** *in vivo*, vaccination experiments were performed in BALB/C female mice bearing 4T1 tumors. The bilateral subcutaneous 4T1 tumor models are ideal cancer vaccine models for antitumor immunotherapy research [50]. 4T1 cells were subcutaneously inoculated to the BALB/C mice as primary tumors. A week later, living 4T1 cells were subcutaneously into the contralateral as distant tumors. 2 days later, the primary tumors were intratumorally injected with **Ru1** and treated with a 425 nm light array (12 J cm^{-2}) after 12 h. The treatment was given every 7 days. The tumor volume and the weight of mice were routinely monitored for 14 days (Fig. 6A).

Compared with the control, the growth of both primary tumors and distant tumors (Fig. 6B and D) is significantly inhibited upon light irradiation. At the end of treatment, the primary tumors and distant tumors in the PDT treatment groups decrease by about 58 % and 84 %, respectively. No significant change in weight of mice was detected, which shows that **Ru1** and **Ru2** possess no obvious side effects (Fig. 6C). Hematoxylin and eosin (H&E) staining of the main organs shows no serious structural and pathological alternations in all the treatment groups (Fig. S30). **Ru1** has a more significant antitumor effect than **Ru2** on both proximal and distal tumors, which may be due to the capability of **Ru1** to self-assemble into NPs for more effective retention in tumors.

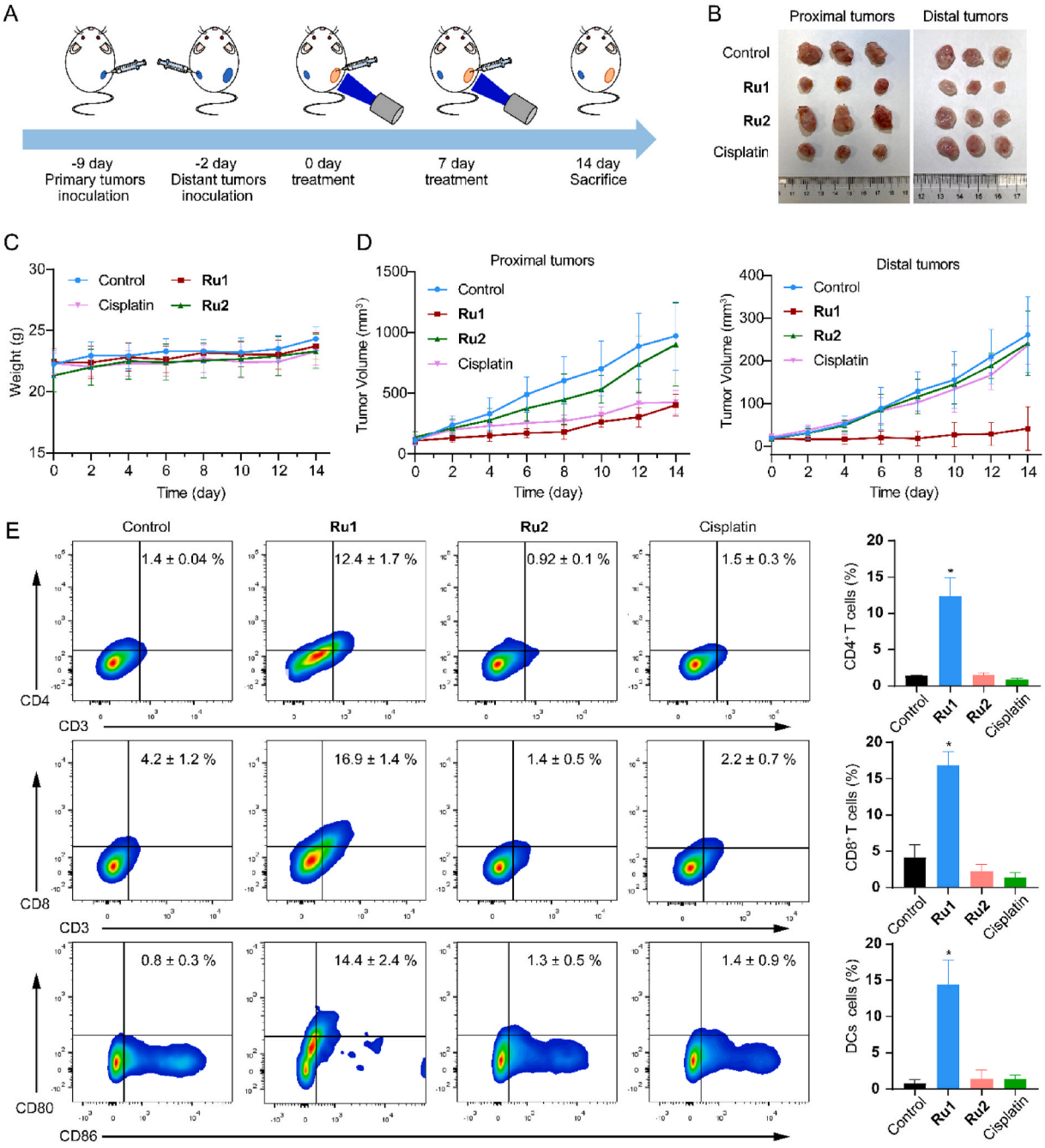

Fig. 6. Ru1 activate cancer immune responses *in vivo*. (A) Schematic diagram of *in vivo* photo-immunotherapy procedure. (B) Representative images of tumors at the end of treatment. (C) The weights of the mice during the treatment. (D) The curves of primary tumor volumes and distant tumor volumes during the treatment. (E) Quantitative measurement of the proportions of $CD8^+$, and $CD4^+$ T cells and cells expressing CD80 and CD86 in tumors at the end of the treatment by flow cytometry (n = 3). Error bars: S.D., n = 3. *$p < 0.05$, **$p < 0.01$, ***$p < 0.001$.

The presence of cytotoxic T cells (CTLs, $CD8^+$ T cells) in tumors is considered to be a specific immune response and is associated with a good prognosis during cancer treatment [60]. The proportions of $CD8^+$ T cells ($CD3^+$ $CD8^+$ T lymphocytes) and $CD4^+$ T cells ($CD3^+$ $CD4^+$ T lymphocytes) are markedly increased in the PDT group. Cells expressing CD86 and CD80 are also increased in the PDT group, which indicates that **Ru1**-mediated PDT can increase the maturation of dendritic cells (DCs; Fig. 6E).

3. Conclusion

We report here a mtDNA-targeted Ru(II) photosensitizer (**Ru1**) that can form self-assembled NPs through intermolecular noncovalent interactions. Due to the formation of NPs, **Ru1** can effectively penetrate into cancer cells through endocytosis. **Ru1** can accumulate in mitochondria and damage mtDNA under visible light irradiation. The cytoplasmic release of dsDNA then effectively activates the cGAS-STING signaling pathway. *In vivo* experiments also demonstrate that the self-assembled **Ru1** NPs possess superior antitumor effects and can markedly improve the cancer immune microenvironments. In all, we report a carrier-free self-assembled photosensitizer for controllable activation of cGAS-STING pathway, which provides ideas for the design of novel cancer photo-immunotherapeutic agents.

CRediT authorship contribution statement

Yu-Yi Ling: Writing – original draft, Visualization, Validation, Methodology, Investigation, Data curation. **Zhi-Yuan Li:** Writing – original draft, Visualization, Validation, Data curation. **Xia Mu:** Writing – original draft, Software, Formal analysis. **Ya-Jie Kong:** Writing – original draft, Visualization, Validation, Data curation. **Liang Hao:** Visualization, Validation, Methodology, Funding acquisition. **Wen-Jin Wang:** Visualization, Methodology, Formal analysis, Data curation. **Qing-Hua Shen:** Visualization, Validation, Software. **Yue-Bin Zhang:** Writing – review & editing, Project administration, Funding acquisition. **Cai-Ping Tan:** Writing – review & editing, Supervision, Project administration, Methodology, Funding acquisition.

Declaration of competing interest

The authors declare that they have no known competing financial interests or personal relationships that could have appeared to influence the work reported in this paper.

Data availability

Data will be made available on request.

Acknowledgements

This study was supported by the National Natural Science Foundation of China (22177142), Basic and Applied Basic Research Foundation of Guangdong Province (Nos. 2024B1515040028) and the Fundamental Research Funds for the Central Universities.

Appendix A. Supplementary data

Supplementary data to this article can be found online at https://doi.org/10.1016/j.ejmech.2024.116638.

References

[1] H. Ishikawa, G.N. Barber, STING is an endoplasmic reticulum adaptor that facilitates innate immune signalling, Nature 455 (2008) 674–678.
[2] G.N. Barber, STING: infection, inflammation and cancer, Nat. Rev. Immunol. 15 (2015) 760–770.
[3] K.-P. Hopfner, V. Hornung, Molecular mechanisms and cellular functions of cGAS-STING signalling, Nat. Rev. Mol. Cell Biol. 21 (2020) 501–521.
[4] Q. Chen, L. Sun, Z.J. Chen, Regulation and function of the cGAS-STING pathway of cytosolic DNA sensing, Nat. Immunol. 17 (2016) 1142–1149.
[5] M. Motwani, S. Pesiridis, K.A. Fitzgerald, DNA sensing by the cGAS-STING pathway in health and disease, Nat. Rev. Genet. 20 (2019) 657–674.
[6] L. Yu, P. Liu, Cytosolic DNA sensing by cGAS: regulation, function, and human diseases, Signal Transduct. Targeted Ther. 6 (2021) 170.
[7] J. Wu, L. Sun, X. Chen, F. Du, H. Shi, C. Chen, Z.J. Chen, Cyclic GMP-AMP is an endogenous second messenger in innate immune signaling by cytosolic DNA, Science 339 (2013) 826–830.
[8] X. Cai, Y.-H. Chiu, Z.-j. Chen, The cGAS-cGAMP-STING pathway of cytosolic DNA sensing and signaling, Mol. Cell 54 (2014) 289–296.
[9] X. Zhang, X.-C. Bai, Z.J. Chen, Structures and mechanisms in the cGAS-STING innate immunity pathway, Immunity 53 (2020) 43–53.
[10] S. Liu, X. Cai, J. Wu, Q. Cong, X. Chen, T. Li, F. Du, J. Ren, Y.-T. Wu, N.V. Grishin, Z.J. Chen, Phosphorylation of innate immune adaptor proteins MAVS, STING, and TRIF induces IRF3 activation, Science 347 (2015) aaa2630.
[11] S. Yum, M. Li, Y. Fang, Z.J. Chen, TBK1 recruitment to STING activates both IRF3 and NF-κB that mediate immune defense against tumors and viral infections, Proc. Natl. Acad. Sci. USA 118 (2021) e2100225118.
[12] Y. Tanaka, Z.J. Chen, STING specifies IRF3 phosphorylation by TBK1 in the cytosolic DNA signaling pathway, Sci. Signal. 5 (2012) ra20.
[13] J. Kwon, S.F. Bakhoum, The cytosolic DNA-sensing cGAS-STING pathway in cancer, Cancer Discov. 10 (2020) 26–39.
[14] N. Samson, A. Ablasser, The cGAS-STING pathway and cancer, Nat. Can. 3 (2022) 1452–1463.
[15] S.-R. Woo, L. Corrales, T.F. Gajewski, The STING pathway and the T cell-inflamed tumor microenvironment, Trends Immunol. 36 (2015) 250–256.
[16] T. Sen, B.L. Rodriguez, L. Chen, C.M.D. Corte, N. Morikawa, J. Fujimoto, S. Cristea, T. Nguyen, L. Diao, L. Li, Y. Fan, Y. Yang, J. Wang, B.S. Glisson, I.I. Wistuba, J. Sage, J.V. Heymach, D.L. Gibbons, L.A. Byers, Targeting DNA damage response promotes antitumor immunity through STING-mediated T-cell activation in small cell lung cancer, Cancer Discov. 9 (2019) 646–661.
[17] A. Decout, J.D. Katz, S. Venkatraman, A. Ablasser, The cGAS-STING pathway as a therapeutic target in inflammatory diseases, Nat. Rev. Immunol. 21 (2021) 548–569.
[18] M.-M. Hu, H.-B. Shu, Mitochondrial DNA-triggered innate immune response: mechanisms and diseases, Cell. Mol. Immunol. 20 (2023) 1403–1412.
[19] M. Kanda, D. Shimizu, K. Sawaki, S. Nakamura, S. Umeda, T. Miwa, H. Tanaka, C. Tanaka, M. Hayashi, Y. Iguchi, S. Yamada, M. Katsuno, Y. Kodera, Therapeutic monoclonal antibody targeting of neuronal pentraxin receptor to control metastasis in gastric cancer, Mol. Cancer 19 (2020) 131.
[20] Y. Wang, J. Luo, A. Alu, X. Han, Y. Wei, X. Wei, cGAS-STING pathway in cancer biotherapy, Mol. Cancer 19 (2020) 136.
[21] K.M. Garland, T.L. Sheehy, J.T. Wilson, Chemical and biomolecular strategies for STING pathway activation in cancer immunotherapy, Chem. Rev. 122 (2022) 5977–6039.
[22] B.A. Flood, E.F. Higgs, S. Li, J.J. Luke, T.F. Gajewski, STING pathway agonism as a cancer therapeutic, Immunol. Rev. 290 (2019) 24–38.
[23] J.M. Ramanjulu, G.S. Pesiridis, J. Yang, N. Concha, R. Singhaus, S.-Y. Zhang, J.-L. Tran, P. Moore, S. Lehmann, H.C. Eberl, M. Muelbaier, J.L. Schneck, J. Clemens, M. Adam, J. Mehlmann, J. Romano, A. Morales, J. Kang, L. Leister, T.L. Graybill, A. K. Charnley, G. Ye, N. Nevins, K. Behnia, A.I. Wolf, V. Kasparcova, K. Nurse, L. Wang, A.C. Puhl, Y. Li, M. Klein, C.B. Hopson, J. Guss, M. Bantscheff, G. Bergamini, M.A. Reilly, Y. Lian, K.J. Duffy, J. Adams, K.P. Foley, P.J. Gough, R. W. Marquis, J. Smothers, A. Hoos, J. Bertin, Design of amidobenzimidazole STING receptor agonists with systemic activity, Nature 564 (2018) 439–443.
[24] E.N. Chin, C. Yu, V.F. Vartabedian, Y. Jia, M. Kumar, A.M. Gamo, W. Vernier, S. H. Ali, M. Kissai, D.C. Lazar, N. Nguyen, L.E. Pereira, B. Benish, A.K. Woods, S. B. Joseph, A. Chu, K.A. Johnson, P.N. Sander, F. Martínez-Peña, E.N. Hampton, T. S. Young, D.W. Wolan, A.K. Chatterjee, P.G. Schultz, H.M. Petrassi, J.R. Teijaro, L. L. Lairson, Antitumor activity of a systemic STING-activating non-nucleotide cGAMP mimetic, Science 369 (2020) 993–999.
[25] B.-S. Pan, S.A. Perera, J.A. Piesvaux, J.P. Presland, G.K. Schroeder, J.N. Cumming, B.W. Trotter, M.D. Altman, A.V. Buevich, B. Cash, S. Cemerski, W. Chang, Y. Chen, P.J. Dandliker, G. Feng, A. Haidle, T. Henderson, J. Jewell, I. Kariv, I. Knemeyer, J. Kopinja, B.M. Lacey, J. Laskey, C.A. Lesburg, R. Liang, B.J. Long, M. Lu, Y. Ma, E. C. Minnihan, G. O'Donnell, R. Otte, L. Price, L. Rakhilina, B. Sauvagnat, S. Sharma, S. Tyagarajan, H. Woo, D.F. Wyss, S. Xu, D.J. Bennett, G.H. Addona, An orally available non-nucleotide STING agonist with antitumor activity, Science 369 (2020) eaba6098.
[26] J. Li, S.M. Canham, H. Wu, M. Henault, L. Chen, G. Liu, Y. Chen, G. Yu, H.R. Miller, V. Hornak, S.M. Brittain, G.A. Michaud, A. Tutter, W. Broom, M.E. Digan, S. M. McWhirter, K.E. Sivick, H.T. Pham, C.H. Chen, G.S. Tria, J.M. McKenna, M. Schirle, X. Mao, T.B. Nicholson, Y. Wang, J.L. Jenkins, R.K. Jain, J.A. Tallarico, S.J. Patel, L. Zheng, N.T. Ross, C.Y. Cho, X. Zhang, X.-C. Bai, Y. Feng, Activation of human STING by a molecular glue-like compound, Nat. Chem. Biol. 20 (2023) 365–372.
[27] K. Yang, W. Han, X. Jiang, A. Piffko, J. Bugno, C. Han, S. Li, H. Liang, Z. Xu, W. Zheng, L. Wang, J. Wang, X. Huang, J.P.Y. Ting, Y.-X. Fu, W. Lin, R. R. Weichselbaum, Zinc cyclic di-AMP nanoparticles target and suppress tumours via endothelial STING activation and tumour-associated macrophage reinvigoration, Nat. Nanotechnol. 17 (2022) 1322–1331.
[28] E.L. Dane, A. Belessiotis-Richards, C. Backlund, J. Wang, K. Hidaka, L.E. Milling, S. Bhagchandani, M.B. Melo, S. Wu, N. Li, N. Donahue, K. Ni, L. Ma, M. Okaniwa,

M.M. Stevens, A. Alexander-Katz, D.J. Irvine, STING agonist delivery by tumour-penetrating PEG-lipid nanodiscs primes robust anticancer immunity, Nat. Mater. 21 (2022) 710–720.
[29] P. Dosta, A.M. Cryer, M.Z. Dion, T. Shiraishi, S.P. Langston, D. Lok, J. Wang, S. Harrison, T. Hatten, M.L. Ganno, V.A. Appleman, G.M. Taboada, N. Puigmal, S. Ferber, S. Kalash, M. Prado, A.L. Rodríguez, W.S. Kamoun, A.O. Abu-Yousif, N. Artzi, Investigation of the enhanced antitumour potency of STING agonist after conjugation to polymer nanoparticles, Nat. Nanotechnol. 18 (2023) 1351–1363.
[30] L. Wang-Bishop, B.R. Kimmel, V.M. Ngwa, M.Z. Madden, J.J. Baljon, D.C. Florian, A. Hanna, L.E. Pastora, T.L. Sheehy, A.J. Kwiatkowski, M. Wehbe, X. Wen, K. W. Becker, K.M. Garland, J.A. Schulman, D. Shae, D. Edwards, M.M. Wolf, R. Delapp, P.P. Christov, K.E. Beckermann, J.M. Balko, W.K. Rathmell, J. C. Rathmell, J. Chen, J.T. Wilson, STING-activating nanoparticles normalize the vascular-immune interface to potentiate cancer immunotherapy, Sci. Immunol. 8 (2023) eadd1153.
[31] Z. Luo, X. Liang, T. He, X. Qin, X. Li, Y. Li, L. Li, X.J. Loh, C. Gong, X. Liu, Lanthanide-nucleotide coordination nanoparticles for STING activation, J. Am. Chem. Soc. 144 (2022) 16366–16377.
[32] X. Li, S. Khorsandi, Y. Wang, J. Santelli, K. Huntoon, N. Nguyen, M. Yang, D. Lee, Y. Lu, R. Gao, B.Y.S. Kim, C. de Gracia Lux, R.F. Mattrey, W. Jiang, J. Lux, Cancer immunotherapy based on image-guided STING activation by nucleotide nanocomplex-decorated ultrasound microbubbles, Nat. Nanotechnol. 17 (2022) 891–899.
[33] L. Zhao, S.-H. Zhuo, T.-Y. Wang, J.-J. Wu, J.-Y. Su, W.-H. Li, B.-D. Zhang, Y.-M. Li, Cyclic dinucleotide self-assembled nanoparticles as a carrier-free delivery platform for STING-mediated cancer immunotherapy, CCS Chem. 6 (2023) 177–195.
[34] D.W. Felsher, Cancer revoked: oncogenes as therapeutic targets, Nat. Rev. Cancer 3 (2003) 375–379.
[35] T.C. Pham, V.-N. Nguyen, Y. Choi, S. Lee, J. Yoon, Recent strategies to develop innovative photosensitizers for enhanced photodynamic therapy, Chem. Rev. 121 (2021) 13454–13619.
[36] Y. Zhang, B.-T. Doan, G. Gasser, Metal-based photosensitizers as inducers of regulated cell death mechanisms, Chem. Rev. 123 (2023) 10135–10155.
[37] A.M.-H. Yip, K.K.-W. Lo, Luminescent rhenium(I), ruthenium(II), and iridium(III) polypyridine complexes containing a poly(ethylene glycol) pendant or bioorthogonal reaction group as biological probes and photocytotoxic agents, Coord. Chem. Rev. 361 (2018) 138–163.
[38] Y. Wu, S. Li, Y. Chen, W. He, Z. Guo, Recent advances in noble metal complex based photodynamic therapy, Chem. Sci. 13 (2022) 5085–5106.
[39] S. Monro, K.L. Colon, H. Yin, J. Roque 3rd, P. Konda, S. Gujar, R.P. Thummel, L. Lilge, C.G. Cameron, S.A. McFarland, Transition metal complexes and photodynamic therapy from a tumor-centered approach: challenges, opportunities, and highlights from the development of TLD1433, Chem. Rev. 119 (2019) 797–828.
[40] H. Yang, R. Liu, Y. Xu, L. Qian, Z. Dai, Photosensitizer nanoparticles boost photodynamic therapy for pancreatic cancer treatment, Nano-Micro Lett. 13 (2021) 35.
[41] Y. Li, M. Zhang, H. Han, B. Zhang, J.B. Matson, D. Chen, W. Li, Y. Wang, Peptide-based supramolecular photodynamic therapy systems: from rational molecular design to effective cancer treatment, Chem. Eng. J. 436 (2022) 135240.
[42] E.J. Hong, D.G. Choi, M.S. Shim, Targeted and effective photodynamic therapy for cancer using functionalized nanomaterials, Acta Pharm. Sin. B 6 (2016) 297–307.
[43] S. Md, S. Haque, T. Madheswaran, F. Zeeshan, V.S. Meka, A.K. Radhakrishnan, P. Kesharwani, Lipid based nanocarriers system for topical delivery of photosensitizers, Drug Discov. Today 22 (2017) 1274–1283.
[44] Y. Shi, R. van der Meel, X. Chen, T. Lammers, The EPR effect and beyond: strategies to improve tumor targeting and cancer nanomedicine treatment efficacy, Theranostics 10 (2020) 7921–7924.
[45] D. Chenthamara, S. Subramaniam, S.G. Ramakrishnan, S. Krishnaswamy, M. M. Essa, F.-H. Lin, M.W. Qoronfleh, Therapeutic efficacy of nanoparticles and routes of administration, Biomater. Res. 23 (2019) 20.
[46] G. Xu, C. Li, C. Chi, L. Wu, Y. Sun, J. Zhao, X.-H. Xia, S. Gou, A supramolecular photosensitizer derived from an arene-Ru(II) complex self-assembly for NIR activated photodynamic and photothermal therapy, Nat. Commun. 13 (2022) 3064.
[47] X.-Q. Zhou, M. Xiao, V. Ramu, J. Hilgendorf, X. Li, P. Papadopoulou, M.A. Siegler, A. Kros, W. Sun, S. Bonnet, The self-assembly of a cyclometalated palladium photosensitizer into protein-stabilized nanorods triggers drug uptake in vitro and in vivo, J. Am. Chem. Soc. 142 (2020) 10383–10399.
[48] X.-Q. Zhou, P. Wang, V. Ramu, L. Zhang, S. Jiang, X. Li, S. Abyar, P. Papadopoulou, Y. Shao, L. Bretin, M.A. Siegler, F. Buda, A. Kros, J. Fan, X. Peng, W. Sun, S. Bonnet, In vivo metallophilic self-assembly of a light-activated anticancer drug, Nat. Chem. 15 (2023) 980–987.
[49] N. Song, Z. Zhang, P. Liu, Y.W. Yang, L. Wang, D. Wang, B.Z. Tang, Nanomaterials with supramolecular assembly based on AIE luminogens for theranostic applications, Adv. Mater. 32 (2020) 2004208.
[50] Y. Zheng, X.-X. Chen, D.-Y. Zhang, W.-J. Wang, K. Peng, Z.-Y. Li, Z.-W. Mao, C.-P. Tan, Activation of the cGAS-STING pathway by a mitochondrial DNA-targeted emissive rhodium(III) metallointercalator, Chem. Sci. 14 (2023) 6890–6903.
[51] Y.-Y. Ling, X.-Y. Xia, L. Hao, W.-J. Wang, H. Zhang, L.-Y. Liu, W. Liu, Z.-Y. Li, C.-P. Tan, Z.-W. Mao, Simultaneous photoactivation of cGAS-STING pathway and pyroptosis by platinum(II) triphenylamine complexes for cancer immunotherapy, Angew. Chem. Int. Ed. 61 (2022) e202210988.
[52] C. Tan, S. Lai, S. Wu, S. Hu, L. Zhou, Y. Chen, M. Wang, Y. Zhu, W. Lian, W. Peng, L. Ji, A. Xu, Nuclear permeable ruthenium(II) β-carboline complexes induce autophagy to antagonize mitochondrial-mediated apoptosis, J. Med. Chem. 53 (2010) 7613–7624.
[53] B. Luo, X. Song, A comprehensive overview of β-carbolines and its derivatives as anticancer agents, Eur. J. Med. Chem. 224 (2021) 113688.
[54] W.-J. Wang, X. Mu, C.-P. Tan, Y.-J. Wang, Y. Zhang, G. Li, Z.-W. Mao, Induction and monitoring of DNA phase separation in living cells by a light-switching ruthenium complex, J. Am. Chem. Soc. 143 (2021) 11370–11381.
[55] J.M. Hope, J.J. Wilson, S.J. Lippard, Photoluminescent DNA binding and cytotoxic activity of a platinum(II) complex bearing a tetradentate β-diketiminate ligand, Dalton Trans. 42 (2013) 3176–3180.
[56] T. Sarwar, S.U. Rehman, M.A. Husain, H.M. Ishqi, M. Tabish, Interaction of coumarin with calf thymus DNA: deciphering the mode of binding by in vitro studies, Int. J. Biol. Macromol. 73 (2015) 9–16.
[57] J. Kypr, I. Kejnovská, D. Renciuk, M. Vorlícková, Circular dichroism and conformational polymorphism of DNA, Nucleic Acids Res. 37 (2009) 1713–1725.
[58] A.P. West, G.S. Shadel, Mitochondrial DNA in innate immune responses and inflammatory pathology, Nat. Rev. Immunol. 17 (2017) 363–375.
[59] L.J. Mah, A. El-Osta, T.C. Karagiannis, γH2AX: a sensitive molecular marker of DNA damage and repair, Leukemia 24 (2010) 679–686.
[60] H. Raskov, A. Orhan, J.P. Christensen, I. Gögenur, Cytotoxic $CD8^+$ T cells in cancer and cancer immunotherapy, Br. J. Cancer 124 (2020) 359–367.